NJC

ROYAL SOCIETY OF CHEMISTRY

PAPER

View Article Online
View Journal | View Issue

Cite this: *New J. Chem.*, 2024, **48**, 12609

A photochromic metal–organic framework with a rare 3D self-interpenetrated architecture and an ultrahigh MnO_4^- sensing ability†

Jinfang Zhang, *[a] Yinlong Yue,[a] Xingyu Tao,[a] Jiarun Zhang,[a] Dejing Yin[b] and Chi Zhang*[ac]

Received 7th May 2024,
Accepted 15th June 2024

DOI: 10.1039/d4nj02133a

rsc.li/njc

Photochromic materials have shown a wide range of applications. However, the development of new photochromic materials is still a great challenge. In this work, a photochromic functional ligand, 9,10-bis(di(pyridine-4-yl)methylene)-9,10-dihydroanthracene (**L**), was selected to construct a photochromic LMOF, $[Ni_2\mathbf{L}(OBA)_2(H_2O)_{1.5}\cdot 3.5i\text{-}PrOH]_n$ (**1**) (LMOF = luminescent metal–organic framework; H_2OBA = 4,4′-oxybisbenzoic acid; i-PrOH = isopropanol). **1** is composed of 4-connected Ni^{2+}, 4-connected **L** and OBA^{2-} bridges and exhibits a rare three-dimensional (3D) (4,4)-connected self-interpenetrated architecture and excellent water, pH and thermal stabilities. **1** and **1′** (**1** after photochromism) can sense MnO_4^- in H_2O by luminescence quenching effects. More importantly, this material after photochromism exhibits ultrahigh sensitivity for detecting MnO_4^- (the second highest K_{sv} of 6.11 × 10^5 M^{-1} and the nearly lowest LOD of 3.96 × 10^{-8} M) and can very efficiently recognize MnO_4^-. The sensing mechanism was explored in detail.

Introduction

Metal–organic frameworks (MOFs) have unique structures[1–4] and extensive applications, such as sensing,[5–9] catalysis,[10–12] adsorption,[13] separation,[14–17] biomedical imaging,[18–20] *etc.* Photochromic MOFs are an important type of MOFs and have very promising applications, such as metal oxidation state modulation,[21] erasable printing without ink,[22] conductivity,[23] anticounterfeiting,[24] sensing,[25,26] *etc.* Photochromic functional units play a decisive role in the construction of photochromic MOFs. Photochromic molecules show significantly different absorption spectra before and after light irradiation, so the incorporation of photochromic ligands into MOFs typically results in different absorptions and/or emissions, resulting in multi-response and/or enhanced properties.

In modern industrial society, many pollutants cause harm to human health and the ecological environment. The MnO_4^- anion is a common strong oxidant in laboratories and factories, which is harmful to organisms and the environment.[27,28] The U. S. Environmental Protection Agency (EPA) has listed MnO_4^- as an important pollutant.[29,30] MnO_4^- is widely used in the fishing and aquaculture industries.[31,32] But excess MnO_4^- is carcinogenic to cells and leads to all sorts of cancer disease.[33] Thus, it is very necessary to develop convenient and efficient methods to detect MnO_4^-. Luminescent metal–organic frameworks (LMOFs) have exhibited obvious advantages in the sensing field.[34–37] Organic ligands will significantly affect the functions of MOFs. Therefore, it is important for the development of special functional organic ligands to construct LMOF-based MnO_4^- sensing materials, but faces huge challenges.

Recently, our group developed new diarylethene-type photochromic organic ligands to construct LMOF-based sensing materials.[38–40] For example, $\{[Cd_{1.5}(\mathbf{L})(HOBA)(EtOH)(SO_4)(H_2O)]\cdot 3H_2O\}_n$ (**a**)[38] and $[Cd_2\mathbf{L}(HBTC)_2\cdot 2H_2O\cdot 2i\text{-}PrOH]_n$ (**b**)[39] are fabricated using a new dihydroanthracene-based photochromic ligand **L**. **a** has a 1D triple-chain architecture and can sense MnO_4^- with extremely high sensitivity and good selectivity after photochromism. **b** shows a 2D (4,6)-connected structure and efficient MnO_4^- sensing ability after photochromism. Herein, a new photochromic luminescent Ni(II)–organic framework $[Ni_2\mathbf{L}(OBA)_2(H_2O)_{1.5}\cdot 3.5i\text{-}PrOH]_n$ (**1**) was constructed using **L**. This MOF shows a more complicated three-dimensional (3D) self-interpenetrated structure and can detect MnO_4^- in H_2O before and after photochromism. Especially, **1′** (**1** after photochromism) has the second highest K_{sv} and nearly lowest LOD values, and can identity MnO_4^- in the presence of $Cr_2O_7^{2-}$.

[a] *International Joint Research Center for Photoresponsive Molecules and Materials, School of Chemical and Material Engineering, Jiangnan University, Wuxi 214122, P. R. China. E-mail: zjf260@jiangnan.edu.cn, chizhang@jiangnan.edu.cn*
[b] *School of Biotechnology, Jiangnan University, Wuxi 214122, P. R. China*
[c] *School of Chemical Science and Engineering, Tongji University, Shanghai 200092, P. R. China*

† Electronic supplementary information (ESI) available. CCDC 2351838. For ESI and crystallographic data in CIF or other electronic format see DOI: https://doi.org/10.1039/d4nj02133a

Table 1 Crystallographic data and structure refinement details of **1**

Compound	**1**
Molecular formula	$C_{74.50}H_{71}N_4Ni_2O_{15}$
Formula weight	1379.77
Temperature (K)	296.15(10)
Wavelength (Å)	1.54178
Crystal system	Monoclinic
Space group	$P2_1/c$ (14)
a (Å)	14.8356(6)
b (Å)	17.6855(8)
c (Å)	27.7286(13)
V (Å^3)	7015.5(5)
Z	4
ρ_{calc}/Mg m^{-3}	1.306
μ/mm^{-1}	1.227
F(000)	2888
Reflections collected	78 514
Unique reflections	14 264
R_{int}	0.0625
No. of parameters	1189
GOF	1.030
R_1 [$I > 2\sigma(I)$]	0.0689
wR_2 [$I > 2\sigma(I)$]	0.2044
$\Delta\rho_{max}/\Delta\rho_{min}$ (e Å^{-3})	0.90/−0.64

Experimental section

Materials and methods

The photochromic organic ligand **L** was synthesized according to a literature method.[38] The chemicals used in this work were purchased directly (Table S1, ESI†). Thermogravimetric analysis (TGA) curves were collected on a TGA/1100SF analyzer. Powder X-ray diffraction (PXRD) patterns were obtained on a Bruker D8 Advance X-ray diffractometer. Simulated PXRD patterns were achieved using Mercury. UV-vis absorption spectra were acquired on a TU-1901 double-beam spectrophotometer. FT-IR spectra were obtained using a Nicolet Impact 470 FT-IR spectrometer with KBr pellets. Fluorescence spectra were recorded using a PTI QM-TM fluorescence spectrometer.

Preparation of 1

$Ni(NO_3)_2{\cdot}6H_2O$ (0.10 mmol, 0.0290 g), **L** (0.05 mmol, 0.0256 g), H_2OBA (0.10 mmol, 0.0258 g), H_2O (3 mL) and i-PrOH (3 mL) were taken in a Teflon-lined stainless-steel vessel, stirred and then heated at 140 °C for 72 h. Then the mixture was cooled to room temperature at a rate of 5 °C h^{-1}. The green crystals were collected and dried in air (yield: 51% based on **L**). IR (cm^{-1}): 3378(s); 3059(s); 2957(s); 1590(vs); 1520(s); 1417(vs); 1387(vs); 1239(vs); 1153(vs); 1090(m); 950(s); 880(s); 782(s); 660(m).

Single crystal structure

A single crystal of **1** was selected to measure its structure using a D8 VENTURE CMOS X-ray diffractometer with Cu Kα radiation. The cell parameter was refined on all observed reflections by using the program APEX-3. Then the structure of **1** was determined by the direct method and refined using the SHELXTL program.[41] All non-hydrogen atoms were anisotropically refined. Single-crystal diffraction experiment and refinement data of **1** are listed in Table 1 (CCDC number: 2351838†).

Luminescence detection experiments

Before performing luminescence sensing experiments, the synthesized crystals were gradually ground in a mortar to reduce their size, which could directly enhance the dispersibility of **1** in water. 1 mg of **1** was dispersed in 40 mL of water, sonicated for 45 min, and left in the dark for 72 h to form a stable suspension (0.025 mg mL^{-1}). After irradiating the H_2O suspension of **1** under 365 nm ultraviolet light for 45 min and standing for 3 days, a stable suspension of **1′** was obtained (0.025 mg mL^{-1}).

Luminescent signals were collected with or without anions in the H_2O suspension of **1** or **1′** for 2 min at 2 mL, including F^-, Cl^-, Br^-, I^-, CO_3^{2-}, HCO_3^-, SO_4^{2-}, NO_3^-, PO_4^{3-}, HPO_4^{2-}, $H_2PO_4^-$, $Cr_2O_7^{2-}$ and MnO_4^-. The dependence of spectral intensity on concentration was analyzed by gradually adding anions into the H_2O suspension of **1** and **1′**. Detailed titration experiments were carried out using a stepwise addition method. 1 mM MnO_4^- aqueous solution was gradually added into 2 mL of H_2O suspension of **1** and 0.1 mM MnO_4^- aqueous solution was gradually added into 2 mL of H_2O suspension of **1′**, respectively. When excited at 350 nm, the emission spectrum of **1** was recorded from 370 nm to 600 nm. Under excitation of 400 nm, **1'** is emitted in the range of 420–620 nm.

Results and discussion

Crystal structure of 1

Single-crystal structural analysis demonstrates that **1** belongs to a monoclinic crystal system with a $P2_1/c$ space group (Table 1)

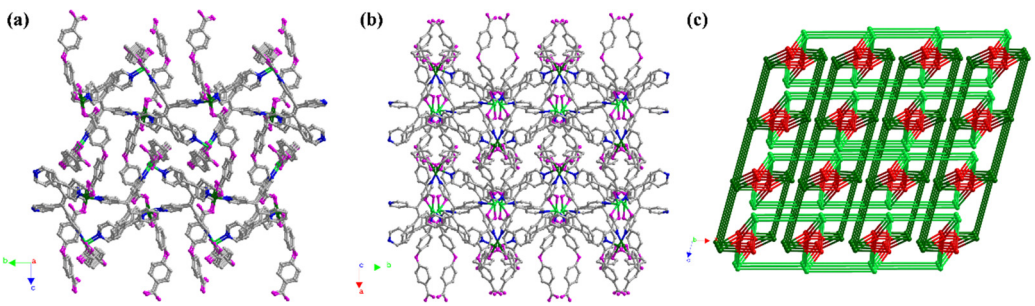

Fig. 1 Self-interpenetrated 3D framework of **1** along the *a*-axis (a) and *c*-axis (b) (Ni1, bright green; Ni2, sea green; N, blue; O, pink; and C, grey). (c) Topology of **1** (Ni1 node, bright green; Ni2 node, sea green; and **L** node, red).

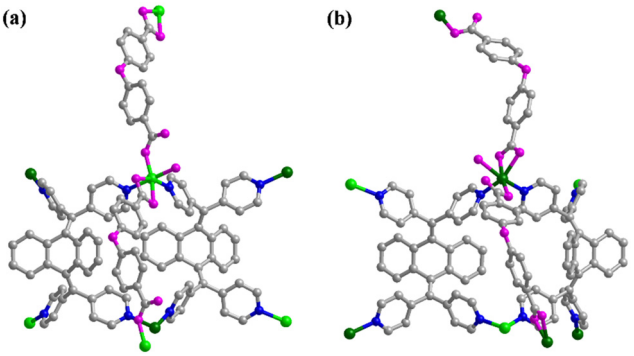

Fig. 2 Coordination and connection of Ni1(II) (a) and Ni2(II) (b) (Ni1, bright green; Ni2, sea green; N, blue; O pink; and C, grey).

and exhibits a self-interpenetrated 3D (4,4)-connected framework, which is composed of 4-connected Ni^{2+}, 4-connected **L** units and OBA^{2-} bridges (Fig. 1 and 2). As shown in Fig. S1 (ESI†), the asymmetric unit of **1** contains two Ni^{2+}, one **L**, two OBA^{2-}, one and a half H_2O and three and a half i-PrOH units. The two kinds of crystals are independent Ni^{2+} with the same coordination environment. Each Ni^{2+} coordinates with four O atoms from two OBA^{2-} and two N atoms from different **L** ligands and one water molecule to form a six-coordinated octahedral pattern (Fig. 2). Each **L** coordinates with two Ni1 and two Ni2 by N atoms from four pyridyl groups (Fig. S2a, ESI†). The dihydroanthracene group is heavily twisted. The angles between two pyridyl groups in one side of dihydroanthracene are 113.833° and 112.056°, which are similar to those from **a** (116.117° and 111.644°) and **b** (113.793° and 108.01°).

Two OBA^{2-} units show the same coordination and connection manners. Each OBA^{2-} bonds with one Ni^{2+} by one carbonyl O atom and chelates with one Ni^{2+} by two O atoms from another side carbonyl (Fig. S2b, ESI†). Therefore, each OBA^{2-} unit is in a μ_2-$\eta^1\eta^1\eta^1$ manner. The lengths of the Ni–N and Ni–O bonds range from 2.047(3) Å to 2.111(3) Å and 2.006(2) Å to 2.207(3) Å, respectively.

OBA^{2-} bridges connect with Ni1 or Ni2 in a μ_2-$\eta^1\eta^1\eta^1$ manner, which results in 1D chains along the *a*-axis or *c*-axis (Fig. 3 and Fig. S3a, b, ESI†). Each **L** links with two Ni1 and two Ni2 and acts as 4-connected units through its four pyridine groups to form a 1D double-chain architecture along the *b*-axis (Fig. 3 and Fig. S3c, ESI†). 1D chains fabricated by OBA^{2-} and Ni1/Ni2 connect with 1D double-chains constructed using **L**, Ni1 and Ni2 units to form a 3D framework (Fig. 3). Interestingly, 1D chains fabricated by OBA^{2-} and Ni1/Ni2 units interpenetrate each other in this 3D framework (Fig. 4).

L connects with two Ni1 and two Ni2 in a 4-connected manner. Each Ni1/Ni2 links with two L units and another two NI1/Ni2 and is still in a 4-connected manner. From the perspective of topology, **L** and Ni1/Ni2 units can be regarded as 4-connected nodes. The Schlafli vertex symbols are $4^2.6^2.8^2$ and $4.6^4.8$ for **L** and Ni1/Ni2 nodes, respectively. Therefore, **1** has a binodal (4,4)-connected topology with a Schlafli symbol of $(4^2.6^2.8^2)(4.6^4.8)_2$ (Fig. 1c). A lot of self-interpenetrated MOFs have been reported;[42,43] however, this binodal (4,4)-connected topology with a Schlafli symbol of $(4^2.6^2.8^2)(4.6^4.8)_2$ is very scarce.[44,45]

Previously, **L** was used by our group to construct two MOFs, $\{[Cd_{1.5}(L)(HOBA)(EtOH)(SO_4)(H_2O)]\cdot 3H_2O\}_n$ (**a**)[38] and $[Cd_2\mathbf{L}(HBTC)_2\cdot 2H_2O\cdot 2i\text{-}PrOH]_n$ (**b**).[39] They show a 1D triple chain and a 2D (4,6)-connected network, respectively. However, **1** features a more complicated 3D self-interpenetrated (4,4)-connected structure. **L** acts as a 4-connected building unit in these MOFs. The involvement of large coordinated molecules (EtOH and SO_4^{2-}) and rigid $HBTC^{2-}$ in **a** and **b** should limit the extension of their structure. **1** has a small H_2O coordinated molecule and long and flexible OBA^{2-} bridges, which results in a 3D self-interpenetrated architecture.

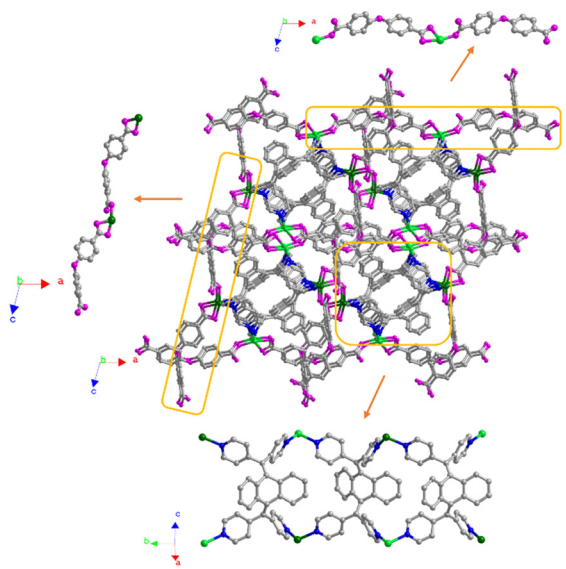

Fig. 3 Formation of the self-interpenetrated 3D framework.

PXRD and TGA

The PXRD pattern of **1** shows good agreement with the simulated pattern from its single crystal data, which proves that **1** has a highly pure phase (Fig. S4, ESI†). The PXRD pattern of **1′** can agree well with that of **1** (Fig. S4, ESI†), which reveals that **1′** and **1** are isomorphic. After soaking in water for 7 days, the PXRD pattern and the mass of **1** have almost no changes (Fig. S4 and S5, ESI†), indicating the excellent water stability of **1**. **1** was immersed in solutions with different pH values for 24 h. The PXRD patterns of **1** agree well with the original pattern within the pH range of 3–11 (Fig. S6, ESI†). As shown in Fig. S7 (ESI†), in a N_2 atmosphere, **1** loses its solvent isopropanol and coordinated water before 159 °C, but the framework can remain unchanged up to 338 °C. Therefore, **1** exhibits excellent water, pH and thermal stabilities.

Photochromism and luminescence of 1

The light green crystals were collected and dried in air (Fig. S8a, ESI†). After being irradiated under UV light, the color of the crystals after soaking in H_2O changed from green to yellow

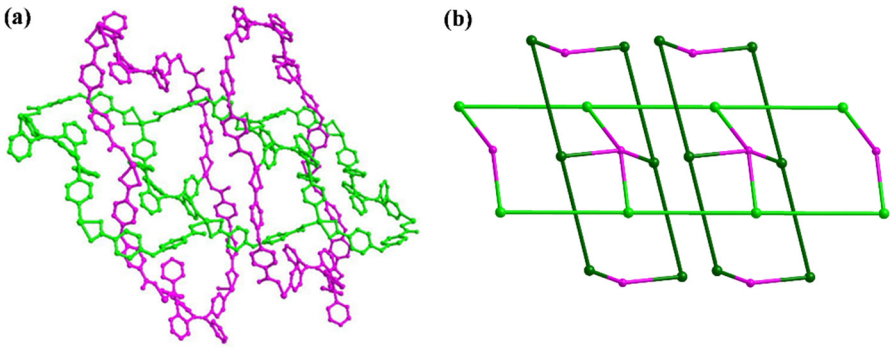

Fig. 4 Self-interpenetrated structure and topology.

(Fig. S8b and c, ESI†). This is an obvious photochromic phenomenon. The suspension of **1** shows excitation and emission at 350 nm and 469 nm, respectively (Fig. 5). The color of the H_2O suspension of **1** is colorless. After being irradiated under UV light, the colorless suspension turns its color to yellow. The suspension of **1′** shows a new excitation peak at 400 nm and the corresponding emission peak at 504 nm (Fig. 5). This indicates that the excitation and emission wavelengths are red-shifted. The photochromism from **1** to **1′** should be attributed to photocyclodehydrogenation of **L** units.[38]

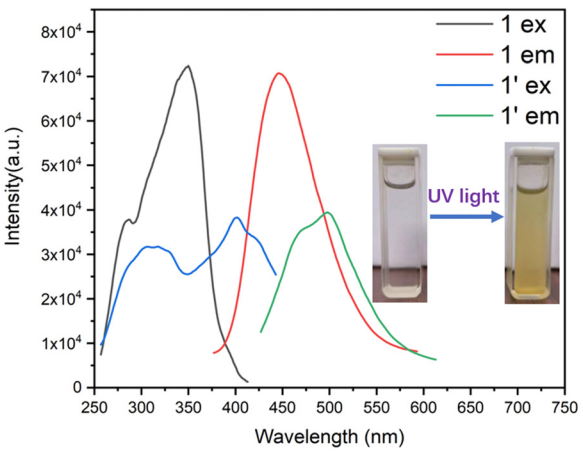

Fig. 5 Excitation and emission of **1** and **1′**.

MnO_4^- sensing

A 50 μL solution with different anions (5 mM) was added into 2 mL H_2O suspensions of **1** and **1′**. As shown in Fig. 6, MnO_4^- and $Cr_2O_7^{2-}$ can quench the emission of the suspension of **1**. Only MnO_4^- can quench the emission of the suspension of **1′**. Therefore, **1** and **1′** can act as promising MnO_4^- sensing materials. Titration experiments of **1** and **1′** toward 1 mM and 0.1 mM solutions of MnO_4^- were carried out, respectively (Fig. 7a and 8a).

The quenching efficiency can be quantitatively analyzed using the Stern–Volmer (S–V) equation: $I_0/I = 1 + K_{sv} \times [M]$. The K_{sv} value of **1** for MnO_4^- is found to be $8.32 \times 10^4\ M^{-1}$ (Fig. 7b). In addition, $3\sigma/k$ (where σ represents the standard deviation and k represents the slope) is used to calculate the LOD. The LOD value of **1** for detecting MnO_4^- is calculated as 1.07×10^{-7} M (Fig. 7c). But the K_{sv} and LOD values of **1′** for detecting MnO_4^- are found to be $6.11 \times 10^5\ M^{-1}$ and 3.96×10^{-8} M, respectively (Fig. 8b and c). The K_{sv} value of **1′** is over 7 times higher than that of **1**, and the LOD value of **1′** is about 3 times lower than that of **1**. More importantly, the LOD value of **1′** reaches the nearly lowest level; the K_{sv} value of **1′** is the second highest in the reported MOF-based MnO_4^- sensors (Table 2). Therefore, **1′** has ultrahigh MnO_4^- sensing sensitivity. The emission intensities and PXRD patterns of **1** (Fig. S9, ESI†) and **1′** (Fig. S10, ESI†) remain basically unchanged after 4 cycles of MnO_4^- sensing, which reveals their good MnO_4^- sensing recyclability.

100 μL of 5 mM H_2O solution of anions was added to 2 mL of a stable water suspension of **1**. These anions, except for $Cr_2O_7^{2-}$,

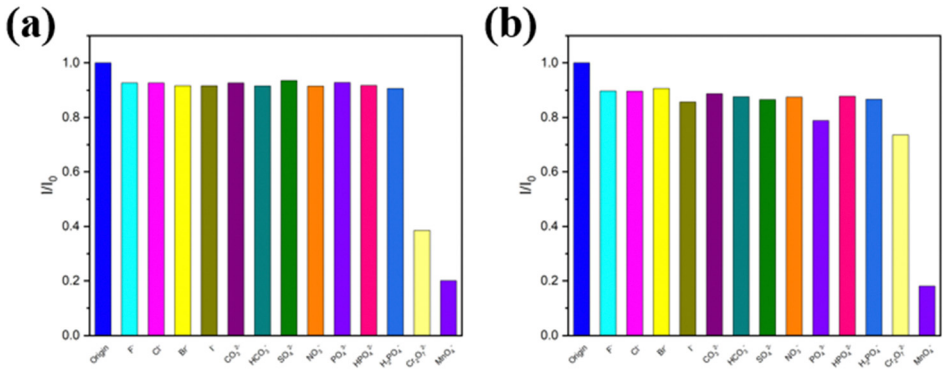

Fig. 6 Quenching efficiency of 1 (a) and **1′** (b) upon addition of different anions.

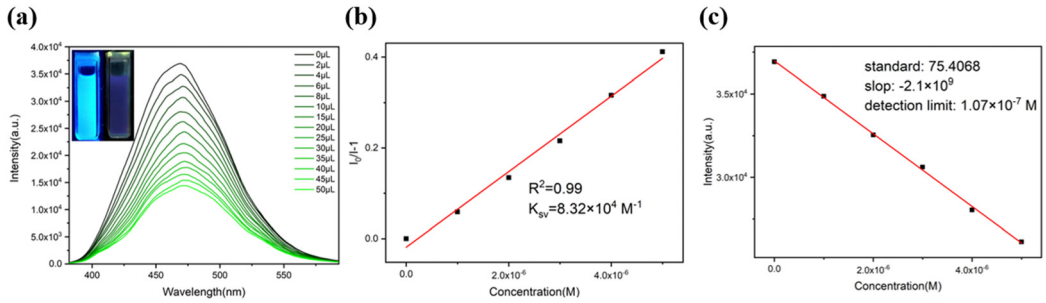

Fig. 7 (a) Emissions of **1** dispersed in H_2O with the addition of MnO_4^- aqueous solution (1 mM) (λ_{ex} = 350 nm and λ_{em} = 469 nm). (b) S–V plot of **1** for sensing MnO_4^-. (c) LOD of **1** for sensing MnO_4^-.

only slightly quenched the emission of **1**. $Cr_2O_7^{2-}$ can quench the emission of **1**. When the same volume of H_2O solution of MnO_4^- (1 mM) was added into the above suspensions, the emission of **1** was obviously quenched (Fig. 9a). And for **1′**, these anions only slightly quenched the emission of **1′**. While the same volume of 0.1 mM MnO_4^- solution was added into the above suspensions, the emission of **1′** was apparently quenched. So **1′** had excellent MnO_4^- sensing selectivity (Fig. 9b).

Sensing mechanism

The PXRD patterns of **1** and **1′** are consistent before and after detecting MnO_4^- (Fig. S4, ESI†), which shows that the frameworks of **1** and **1′** have not collapsed before and after detecting MnO_4^-. The crystal shapes of **1** and **1′** after detecting MnO_4^- have no changes (Fig. S7d and e, ESI†). A clear overlap can be observed between the excitation of **1** (260–400 nm) and the absorption of $Cr_2O_7^{2-}$ (320–400 nm) and MnO_4^- (320–410 nm) (Fig. 10), which leads to competitive energy absorption between $Cr_2O_7^{2-}$/MnO_4^- and **1**. As a result, both $Cr_2O_7^{2-}$ and MnO_4^- cause the emission quenching of **1**. Accordingly, **1** cannot recognize MnO_4^- in the presence of $Cr_2O_7^{2-}$. The new excitation band (350–450 nm) of **1′** overlaps well with the absorption band of MnO_4^- (320–460 nm) and deviates from the absorption bands of $Cr_2O_7^{2-}$ (320–400 nm) (Fig. 10). Thus, competitive energy absorption can occur only between **1′** and MnO_4^-. An efficient FRET will occur between **1′** and MnO_4^- due to a good overlap between the emission of **1′** (420–600 nm) and another absorption band (500–600 nm) of MnO_4^- (Fig. 10). These cause ultrahigh MnO_4^- sensing sensitivity and efficient selectivity for **1′**.

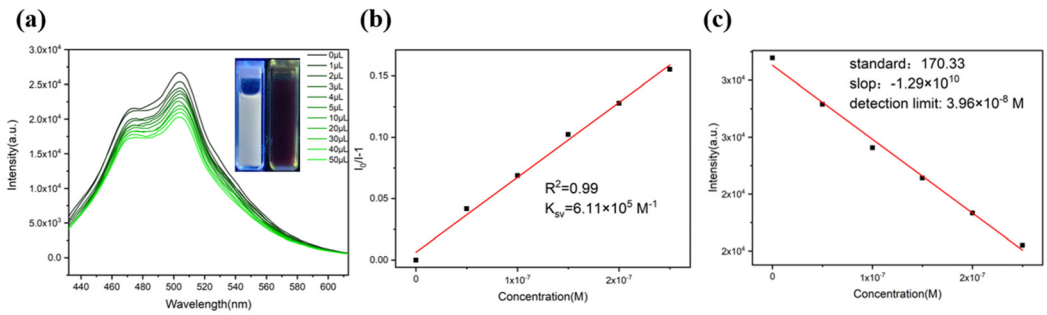

Fig. 8 (a) Emissions of **1′** dispersed in H_2O with the addition of MnO_4^- aqueous solution (0.1 mM) (λ_{ex} = 400 nm and λ_{em} = 504 nm). (b) S–V plot of **1′** for sensing MnO_4^-. (c) LOD of **1′** for sensing MnO_4^-.

Table 2 Luminescent MOF-based MnO_4^- sensors in aqueous medium

	K_{sv} (M^{-1})	LOD (mM)	Ref.
1	8.32×10^4	1.07×10^{-4}	This work
1′	6.11×10^5	3.96×10^{-5}	This work
$\{[Cd_{1.5}(L)(HOBA)(EtOH)(SO_4)(H_2O)]\cdot 3H_2O\}_n$	3.74×10^6	4.11×10^{-5}	38
$[Cd_2L(HBTC)_2\cdot 2H_2O\cdot 2i\text{-}PrOH]_n$	4.08×10^5	9.33×10^{-5}	39
$\{Zn(L)(TPA)\cdot H_2O\}_n$	1.16×10^5	8.0×10^{-4}	40
$\{[Eu_2Na(Hpddb)(pddb)_2(CH_3COO)_2]\cdot 2.5(DMA)\}_n$	2.84×10^3	5.99×10^{-3}	46
$[Zn(L)_2]\cdot 2DMF$	1.92×10^4	2.34×10^{-4}	47
$[(H_2bpp)\cdot[(UO_2)_2]\text{-}(nip)_3]\cdot H_2O$	1.88×10^4	1.79×10^{-3}	48
$\{[Ln_2(L_2)_2(H_2O)_5]\cdot 3H_2O\}_n$	8.47×10^3	1.36×10^{-3}	49
In(OH)bpydc (In-MOF)	2.07×10^5	1.47×10^{-4}	50
TMU-41(OMS)	3.2×10^5	3×10^{-5}	51
$[Ba_3La_{0.5}(\mu_3\text{-}L)_{2.5}(H_2O)_3(DMF)]$	7.73×10^3	2.8×10^{-4}	52

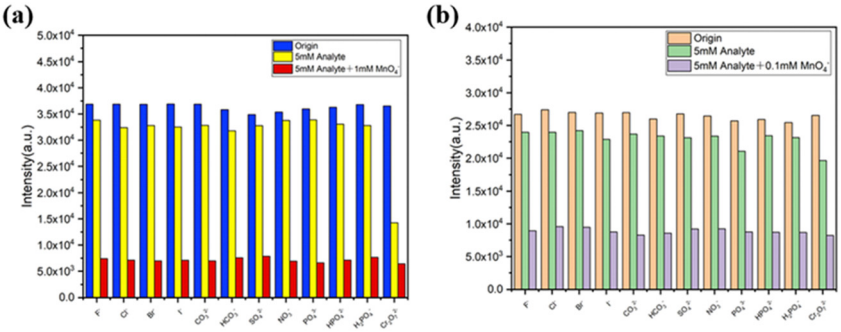

Fig. 9 Selective MnO_4^- detection of **1** (a) and **1′** (b) in the presence of different interfering anions.

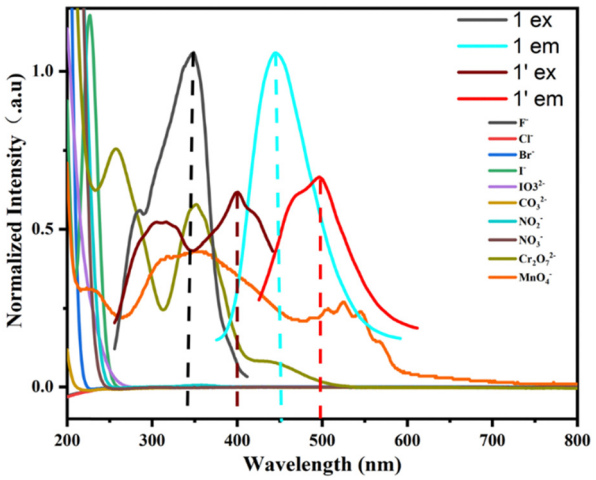

Fig. 10 UV-vis absorption of anions and excitation and emission of **1** and **1′**.

Conclusions

An efficient LMOF-based sensor **1** was successfully constructed using a dihydroanthracene-based photochromic organic ligand. **1** exhibits a rare 3D (4,4)-connected self-interpenetrated architecture and has excellent water, pH and thermal stabilities. **1** and **1′** can detect MnO_4^- in H_2O through luminescence quenching effects. Especially, **1′** has extremely high sensing sensitivity and selectivity toward MnO_4^-. Competitive absorption and FRET should be responsible for the highly efficient MnO_4^- sensing capability of **1′**. This work focuses on the fundamental study of photochromic MOFs including their synthesis, crystal structures, and photochromic, luminescence and sensing properties. This will provide support for the future practical applications of photochromic MOFs such as sensing, anticounterfeiting, *etc.*

Data availability

Crystallographic data for **1** have been deposited at the CCDC under [2351838] and can be obtained from **https://www.ccdc.cam.ac.uk/data_request/cif**.

Conflicts of interest

There are no conflicts of interest to declare.

Acknowledgements

This research was supported by the National Natural Science Foundation of China (21671082 and 51432006) and the 111 Project (B13025).

References

1 Y. Huang, J. Liang, X. Wang and R. Cao, *Chem. Soc. Rev.*, 2017, **46**, 126–157.
2 H. He, J. Perman, G. Zhu and S. Ma, *Small*, 2016, **12**, 6309–6324.
3 B. Li, M. Chrzanowski, Y. Zhang and S. Ma, *Chem. Rev.*, 2016, **307**, 106–129.
4 J. Qin, S. Yuan, C. Lollar, J. Pang, A. Alsalme and H. Zhou, *Chem. Commun.*, 2018, **54**, 4231–4249.
5 B. Zhu, Y. Jin, J. Chu, M. Zuo and S. Cui, *RSC. Adv.*, 2022, **12**, 6951–6957.
6 S. Guo, C. Fan, G. Liu and S. Pu, *RSC. Adv.*, 2018, 8, 39854–39864.
7 J. Zhang, S. Ren, H. Xia, W. Jia and C. Zhang, *J. Mater. Chem. C*, 2020, **8**, 1427–1432.
8 A. Mandal, A. Adhikary and A. Sarkar, *Inorg. Chem.*, 2020, **59**, 17758–17765.
9 H. Yu, Q. Liu and J. Li, *J. Mater. Chem. C*, 2021, **9**, 562–568.
10 J. Gascon, A. Corma and F. Kapteijn, *ACS Catal.*, 2014, **4**, 361–378.
11 S. Rogge, A. Bavykina and J. Hajek, *Chem. Soc. Rev.*, 2017, **46**, 3134–3184.
12 Z. Wang, X. Yue and Q. Xiang, *Coord. Chem. Rev.*, 2024, **504**, 215674.
13 S. Ullah, M. Bustam and M. Assiri, *Microporous and Mesoporous Mater.*, 2020, **294**, 109844.
14 Y. Chen, H. Wu and Y. Yuan, *Chem. Eng. J.*, 2020, **385**, 123836.
15 H. Daglar, H. Gulbalkan and G. Avci, *Angew. Chem., Int. Ed.*, 2021, **60**, 7828–7837.

16 K. Adil, Y. Belmabkhout and R. Pillai, *Chem. Soc. Rev.*, 2017, **46**, 3402–3430.
17 J. Li, J. Sculley and H. Zhou, *Chem. Rev.*, 2012, **112**, 869–932.
18 P. Horcajada, T. Chalati and C. Serre, *Nat. Mater.*, 2010, **9**, 172–178.
19 R. Della, D. Liu and W. Lin, *Acc. Chem. Res.*, 2011, **44**, 957–968.
20 P. Horcajada, R. Gref and T. Baati, *Chem. Rev.*, 2012, **112**, 1232–1268.
21 C. Martin, K. Park, G. Leith, J. Yu, A. Mathur, G. Wilson, G. Gange, E. Barth, R. Ly, O. Manley, K. Forrester, S. Karakalos, M. Smith, T. Makris, A. Vannucci, D. Peryshkov and N. Shustova, *J. Am. Chem. Soc.*, 2022, **144**, 4457–4468.
22 B. Garai, A. Mallick and R. Banerjee, *Chem. Sci.*, 2016, **3**, 2195–2200.
23 H. Wentz, G. Skorupskii, A. Bonfim, J. Mancuso, C. Hendon and E. Oriel, *Chem. Sci.*, 2020, **11**, 1342–1346.
24 S. Venkateswarlu, A. Reddy, A. Panda, D. Sarkar, Y. Son and M. Yoon, *ACS Appl. Nano. Mater.*, 2020, **3**, 3684–3692.
25 Y. Xiu and L. Fei, *J. Mater. Chem. C*, 2015, **3**, 22369–22376.
26 L. Wang, J. He and Q. Yang, *Environ. Pollut.*, 2017, **230**, 902–910.
27 S. Goldhaber, *Regul. Toxicol. Pharmacol.*, 2003, **38**, 232–242.
28 D. Wang, K. Chen, M. Wang, Y. You and X. Zhou, *J. Mol. Struct.*, 2021, **1239**, 130486.
29 B. Stern, *J. Toxicol. Environ. Health, Part A*, 2010, **73**, 114–127.
30 P. Georgopoulos, A. Roy, M. Yonone-Lioy, R. Opiekun and P. Lioy, *J. Toxicol. Environ. Health, Part B*, 2001, **4**, 341–394.
31 S. Ibrahim and A. Al-Hossainy, *J. Mol. Liq.*, 2020, **318**, 114041.
32 S. Ibrahim, A. Al-Hossainy, B. Saha and M. El-Aal, *J. Mol. Struct.*, 2022, **1268**, 133679.
33 Y. Wang, S. Wang and W. Wang, *Spectrochim. Acta, Part A*, 2020, **229**, 117915.
34 J. Ma and W. Liu, *Dalton*, 2019, **48**, 12287–12295.
35 J. Zhang, Q. Qiu and Q. Xiang, *Dyes. Pigments*, 2021, **196**, 109760.
36 Z. Hu, B. Deibert and J. Li, *Chem. Soc. Rev.*, 2014, **43**, 5815–5840.
37 X. Zhang, F. Chen and Q. Wen, *J. Mol. Struct.*, 2022, **1252**, 132183–132190.
38 Z. Lin, W. Li, Q. Chen, L. Chen, C. Zhang and J. Zhang, *J. Mater. Chem. C*, 2022, **10**, 1672–1680.
39 J. Zhang, Z. Lin, Y. Yue, Q. Chen, D. Yin and C. Zhang, *New J. Chem.*, 2023, **47**, 21986–21993.
40 J. Zhang, L. Chen, Q. Chen, Y. Yue, Q. Chen, D. Yin and C. Zhang, *Dyes Pigm.*, 2023, **220**, 111751.
41 G. Sheldrick, *Acta Crystallogr., Sect. C: Struct. Chem.*, 2015, **71**, 3–8.
42 F. Guo, C. Su, Y. Fan, W. Shi and X. Zhang, *Inorg. Chem.*, 2020, **59**, 7135–7142.
43 Y. Qiao, X. Chang, J. Zheng, Z. Chang and M. Yu, *Inorg. Chem.*, 2021, **60**, 2749–2755.
44 P. Zhang, B. Li, Y. Zhao, X. Meng and T. Zhang, *Chem. Commun.*, 2011, **47**, 7722–7724.
45 D. Zhong, L. Liao, J. Deng, Q. Chen, P. Lian and X. Luo, *Chem. Commun.*, 2014, **50**, 15807–15810.
46 B. Li, Q. Yan and G. Yong, *J. Mater. Chem. C*, 2020, **8**, 11786–11795.
47 L. Wang, B. Tu, W. Xu, Y. Fu and Y. Zheng, *Inorg. Chem.*, 2020, **59**, 5004–5017.
48 M. Lee, J. Kim and J. Sessler, *Chem. Soc. Rev.*, 2015, **44**, 4185–4191.
49 Z. Sun, J. Sun, L. Xi, J. Xie, X. Wang, Y. Ma and L. Li, *Cryst. Growth Des.*, 2020, **20**, 5225–5234.
50 J. Wu and B. Yan, *J. Colloid Interface Sci.*, 2017, **504**, 197–205.
51 N. Abdollahi and A. Morsali, *Acta*, 2019, **1064**, 119–125.
52 B. Ding, S. Liu, Y. Cheng, C. Guo, X. Wu, J. Guo, Y. Liu and Y. Li, *Inorg. Chem.*, 2016, **55**, 4391–4402.